

High-Efficiency Photodetector Based On CVD-Grown WS₂ Monolayer

Rakesh K. Prasad¹, Koushik Ghosh², P. K. Giri², Dai-Sik Kim³, Dilip K. Singh^{1*}

¹Department of Physics, Birla Institute of Technology Mesra, Ranchi -835215, India

²Department of Physics, Indian Institute of Technology Guwahati, Assam-781039, India

³Department of Physics and Quantum Photonics Institute and Center for Atom Scale Electromagnetism, Ulsan National Institute of Science and Technology (UNIST), Ulsan-44919, Republic of Korea

*Email: dilipsinghnano1@gmail.com

Abstract

Future generation technologies demand high efficiency photodetectors to enable sensing and switching devices for ultrafast communication and machine vision. This require direct-band gap materials with high photosensitivity, high detectivity and high quantum efficiency. Monolayered two- Dimensional (2D)-Semiconductors based photodetectors are the most promising materials for such applications, although experimental realization has been limited due to unavailability of high quality sample. In the current manuscript, we report about WS₂ based photodetector having sensitivity of 290 AW⁻¹ upon 405 nm excitation and incident power density as low as 0.06 mW/cm². The fabricated device shows detectivity of 52×10^{14} with external quantum efficiency of 89×10^3 %. The observed superior photo-response parameters of CVD grown WS₂ based photodetector as compared to Si-detectors establishes it capability to replace the Si-photodetectors with monolayered ultrathin device having superior performance parameters.

KEYWORDS: Monolayer Tungsten disulfide, 2-Dimensional growth, CVD, High efficiency Photodetectors,

Photodetectors (PDs) are important component to achieve devices with multi-functionality which convert photons into electrical signals. They are widely used for imaging¹, optical communications², sensing³ and in biomedical instruments⁴. There have been overgrowing demand to achieve PDs with enhanced performance in terms of high sensitivity over wide spectral range, faster switching rates and high pixel density requiring small device foot prints. These requirements are further intensified with applications requiring PDs operation under different environments like high temperature, low light conditions requiring extremely high signal/ noise ratio, thermal imaging using PDs for night vision. Meeting these desired properties requires replacement of conventional materials like silicon / Germanium with new materials having direct-band gap structure and strong light matter interaction.

Atomically thin layered materials like graphene and Transition metal dichalcogenides (TMDCs) due to their high photo absorbance properties are considered as one of the potential candidates to achieve efficient PDs^{5,6}. A number of 2D- materials, their hetro-structures and numerous device architectures has been experimentally explored to meet the desired properties^{7,8,9,10}. PDs based on 2D materials have broad electromagnetic spectrum sensitivity as compared to PDs based on traditional bulk semiconductor due to wide bandgap range 0 to 6 eV¹¹. Among wide range of 2D materials, transition metal dichalcogenides (TMDCs) has been explored extensively due to their decent mobility, direct-band gap structure resulting from quantum confinement^{12,13}, high quantum efficiency¹⁴ and the possibility of fabrication of hetro-structures without requirement of epitaxial growth^{6,15}. 2D-TMDs are formed by (Mo, W) transition metals atoms and chalcogenides (S, Se, Te) forming MX₂ semiconductors with a bandgap in the range 1.162.1 eV (visible to infrared) region⁶. The in-plane X-M-X covalent bonds lead to the formation of isolated atomic layers. The individual X-M-X sheets engage with one another via

weak van der Waals forces resulting in bulk crystals^{16,17,18}. In the monolayer limit, these materials apart from showing direct band-gap electronic structure show strong excitonic effects and spin and valley-dependent properties making them highly desirable for photonics and optoelectronics applications¹⁹.

Among the TMDs family of materials, Molybdenum disulfide (MoS₂) and Tungsten disulfide (WS₂) have been most extensively researched for photodetector applications¹⁹. The first monolayered MoS₂-based phototransistor showed good stability and a response time of 50 ms due to low absorbance²⁰. WS₂ shows phonon-limited high electron mobility of 1,103 cm²/ (V.s) at room temperature²¹, broader spectral response as compared to GaAs and Si (less than 1 nm thickness) ^{22,23}. It has high optical absorption coefficient of 10⁵-10⁶ cm⁻¹ ²². It shows layer-dependent band gap of 1.2 ó 2.0 eV ²³ and large exciton binding energies of 700- 800 meV^{14,23}. Monolayered WS₂ shows photoluminescence quantum yield as high as 2 %, which is much higher than that of suspended monolayer MoS₂ 0.42% ²⁴. These properties makes WS₂ preferred material for photodetector applications as compared to other 2D TMDs. In one of the early attempts, photodetector fabricated using mechanically exfoliated WS₂-nanosheets exhibited high responsivity in the range of 0.1 A/W to 5.7 A/W over the spectral range of 370 to 1064 nm^{25,26,27}. Due to the limited lateral dimensions, the devices fabricated using mechanically exfoliated flakes (~100 micrometers) having random shape, thickness and crystal quality shows wide variation in the device properties ²⁶. This limits its use towards imaging pixels and display devices, which normally require large arrays of photodetectors.

Recently, there has been an ongoing effort to grow continuous large crystallite WS₂ using the chemical vapor deposition (CVD) technique ^{24,28,29}, although only a few have been able to demonstrate successful growth of continuous mono-layered WS₂ having quality suitable for the

fabrication of optoelectronic devices³⁰. Unfortunately, the fabricated phototransistor showed poor responsivity limited to 18.8 mA W⁻¹ at 532 nm by applying a high voltage (~ 60V) through the gate channel in the vacuum³¹. Any practical application of a device with such high applied potential (+ 60 V) is not feasible. In another attempt, the three terminal WS₂ photodetectors showed responsivity = 0.52 mA/W, while the photodetector fabricated on the flexible substrate showed responsivity of = 5 mA/W³² with 532 nm laser excitation. Recently, in 2021 Ying Chen fabricated two terminal devices using grown monolayer WS₂ triangular flakes with the high photo-responsivity of 7.3 AW⁻¹ with 500 nm³³. In 2016 Ying Chen et al. grew monolayer WS₂ via Silanization treatment and fabricated two terminal photodetector devices which give responsivity upto 307 AW⁻¹ under 500 nm excitation³⁴. In another report, mechanically exfoliated WS₂ nanoflakes utilizing surface-adsorbates-sensitive charge transport and under NH₃ gas an external quantum efficiency of 884 AW⁻¹ was observed. In the case of CVD grown WS₂ monolayers, the observed limited photosensitivity and slow response time requires further increase in the crystallite size and continuity of the grown material.

In this work, we report about synthesis of large-area continuous films of WS₂ monolayer through CVD and observed superior photo-detection parameters of the fabricated photodetector based on grown WS₂ monolayer.

For WS₂ growth Tungsten trioxide WO₃ 20 mg (99.9 % sigma Aldrich) and sulfur powder 200 mg (99.9% Sigma Aldrich) were used as precursors and carrier gas Ar flow rate was kept at 100 sccm. The schematic of the CVD setup and the parameters of WS₂ growth are shown in supporting Information figure S1. The growth was carried out at 850 °C for 15 minutes using a single zone CVD furnace at atmospheric pressure.

The growth of WS₂ flakes was initially confirmed using an optical microscope (Leica 580) with an objective lens 10× (NA 1.3), 50× (NA 2.6). Detailed morphology of grown samples was recorded using a field emission scanning electron microscope (ZEISS Sigma 300 FESEM). Raman spectroscopy ((LabRam HR800, Jobin Yvon) in the Raman shift range 350-450 cm⁻¹ was used to determine the number of layers of WS₂. Photoluminescence spectra was recorded in the range 500-800 nm using an Ar⁺ ion laser (λ_{ex} = 532 nm). Atomic Force Microscopy (AFM) (Cypher, Oxford Instruments) in noncontact mode was used to measure the thickness and surface topology. WS₂ monolayer-based photodetectors were fabricated using WS₂ on SiO₂ (285 nm)/p-Si wafers. On top of grown WS₂, microelectrodes were fabricated using shadow masking. The gap between adjacent electrodes was maintained at 30 μm. The I-V characteristics and temporal response of the photocurrent were determined using a microprobe station (ECOPIA EPS-500), a 405 nm laser with TTL modulation, and a source meter (Keithley 2400).

Figure 1 (a) shows the optical micrograph of WS₂ grown using CVD. It shows continuous growth over the complete wafer (1.5 × 1.5 cm²) with a coverage area of 98 % calculated using Image J software. It shows small triangular regions of nucleation centers, with dark colour contrast indicating nucleation centers for more than one layer structure. FESEM image, figure 1(b) shows magnified image of as-grown single crystal of WS₂ having size of ~ 80 μm. Figure 1 (c) shows the Atomic Force Microscope (AFM) image of the WS₂ isolated crystal and figure 1(d) shows the thickness profile graph of the WS₂ monolayer is ~ 0.9 nm.

Figure 2(a) shows the Raman spectra of the WS₂-grown sample. Spectra were fitted, using Lorentzian line shape to ascertain the peak profile parameters. It shows peaks at 294.5 cm⁻¹, 323.0 cm⁻¹, 343.1 cm⁻¹, 351.0 cm⁻¹, 355.6 cm⁻¹ and 417.9 cm⁻¹ peaks. The peak at 343.1 cm⁻¹,

355.6 cm^{-1} arises due to first order in-plane vibration $E_{2g}^1(\text{M})$, $E_{2g}^1(\Gamma)$ mode³⁵ and 417.9 cm^{-1} is first order out-of-plane vibration $A_{1g}(\Gamma)$ mode. Other peaks observed at 294.5 cm^{-1} and 323.0 cm^{-1} are attributed to the combination modes of $2\text{LA}-2E_{2g}^2$ and $2\text{LA}-E_{2g}^2$, respectively. The frequency separation of 62.3 cm^{-1} between the $E_{2g}^1(\Gamma)$ and $A_{1g}(\Gamma)$ ²⁸ and the strong $2\text{LA}(\text{M})$ mode at a laser excitation of 532 nm caused by the double resonance scattering could be the spectral fingerprint of monolayer WS_2 .³⁶ The first order Raman spectra of the WS_2 monolayer shows two optical phonon modes at the Brillouin zone center ($E_{2g}^1(\Gamma)$ and $A_{1g}(\Gamma)$) and one longitudinal acoustic mode at the M point $\text{LA}(\text{M})$. $E_{2g}^1(\Gamma)$ was an in-plane optical mode, $A_{1g}(\Gamma)$ correspond to out-of plane vibration of the sulfur atom as the longitudinal acoustic phonons $\text{LA}(\text{M})$ were in σ plane collective movement of the atom. Additional peaks correspond to the second order Raman mode which are multi phonon combination of these first-order modes. Figure 2(b) shows the photoluminescence (PL) spectra from as grown sample along with fitted peaks using Gaussian line shape. Strong PL peak between 600 and 680 nm indicates monolayer WS_2 crystal growth²⁸. The peak has maxima at the wavelength of 632 nm (direct band gap 1.96 eV) which falls in the range of reported PL peak positions for monolayer WS_2 thin film^{18,25,26}. Spectra shows two Gaussian components at 632.5 nm and 638.5 nm arising from A exciton (X) and Trions (X^-)^{37,38}.

The schematic diagram of the fabricated device is shown in Figure 3(a). Figure 3(b) shows the photoresponse of the device under dark and various laser excitation wavelengths: 360 nm with an incident power density (4.65 mW/cm^2), 405 nm (52.3 mW/cm^2), 532 nm (80 mW/cm^2) and 630 nm (2.25 mW/cm^2). The device showed an extremely low dark current (~ 9.5 pA). Figure 3(c) shows the I-V response with varying incident photon density in the range of

0.06 mW/cm² to 75.3 mW/cm² for $\lambda = 405$ nm excitation. The variation in the photocurrent for the applied potential of +5V is shown in Figure 3(d). The photo-induced carrier concentration increases exponentially with increasing incident photon density. The induced photocurrent (I_{ph}) follows $I_{ph} = 5 \times 10^{-7} - I_o \cdot \exp(R \cdot P)$ dependence with $R = -0.821$ and $I_o = 2.062 \times 10^{-7}$. Where P indicates incident power density. The responsivity first increases fast and then saturates with increasing incident power density. Due to the complex interplay of the processes of electron-hole generation, trapping and recombination deviation from the linear dependence is observed. This is different from the previous observation where linear response was observed^{25,26}.

The change in the photocurrent with varying incident laser power ($\lambda = 405$ nm) at a constant bias of 5V is shown in figure 4(a). With increasing irradiation power in the range 0.06 to 75.3 mW/cm², the photocurrent sequentially changes from 10 nA to 0.12 μ A. Through rise and fall time of the photodetector and its dependence on incident laser power irradiations, the dynamic behavior of the photodetector was explored. Observed experimental data of the rise and fall times of the photocurrent ($I(t)$) was fitted using single exponential function given by $I(t) = I_0 + A \exp^{-t/\tau}$, Where I_0 and A are the constants and τ is referred as time constant. The photocurrent growth and decay shows systematic growth with the variation of laser power illumination. The rise time varies from (0.20 to 0.60 sec) and the fall time varies from (0.07 to 0.27 sec) as shown in figure 4(b). Figure 4(c) shows the temporal response of the photocurrent under varying applied bias voltage with a fixed laser power intensity. With increase of bias potential the photocurrent systematically increases. The Rise time varies from (0.18 to 0.83 sec). Interestingly with increasing bias potential upto 3V the rise time sequentially increases and upon further increase of applied bias voltage (to 4V and 5V) the rise time decreases. Similarly the fall time

sequentially increases from 0.07 sec to 0.28 sec with increasing bias voltage for constant illumination power (52.4 mW/cm²).

The performance of the fabricated photodetector is estimated in terms of responsivity (R), detectivity (D*) and external quantum efficiency EQE (%) ³⁹. The responsivity is calculated

using $R_{\lambda} = \frac{I_{Ph}}{P_{in}A}$. Where I_{Ph} represents the photocurrent (I_{Light} - I_{Dark}), P_{in} represents the power density of incident light, A the effective active area and photosensitivity is represented in terms

of ratio I_{ph}/I_{Dark}. Further, detectivity (D*) was calculated using $D^* = \frac{R_{\lambda} \sqrt{A}}{q(I_{ph} + I_{dark})}$. The number of carriers produced per incident photon is expressed as EQE and is calculated: EQE (%) = $(1240 \cdot \frac{R_{\lambda}}{\lambda}) * 100$, Where λ represents the operating wavelength⁴⁰. We observed the responsivity of

290 AW⁻¹ at 405 nm of excitation and with incident power density of 0.06 mW/cm². The observed responsivity is much higher than previously reported values even for the PLD grown samples (0.70 AW⁻¹) due to their poor control of number of layers ²⁵. Few of the experimental

attempts have shown comparable responsivity (100-570 mAW⁻¹) for the bilayers or, multilayer MoS₂ / WS₂ primarily due to increased optical absorption (40-85 %) as compared to the monolayered structures (2-10 %) ^{25,41}. The variation in the responsivity (R), detectivity (D), and

external quantum efficiency (%) with varying incident power density (mW/cm²) and voltage (V) are shown in Figure. 5(a) and Figure 5(b) respectively. At 0.06 mW/cm² the photodetector shows responsivity (290 AW⁻¹), detectivity (52 × 10¹⁴) and external quantum efficiency of 89 × 10³ %.

For the incident power range of 0.1 mW/cm² -10 mW/cm² range responsivity, detectivity and external quantum efficiency remains nearly constant. Detectivity represents the ability to detect weak signals. For estimating detectivity, short noise is assumed to dominate the dark current. Beyond 10 mW/cm² incident power range, these figures of merits monotonically decreases with

increasing incident power density. As the P_{in} increases, more holes fill shallow trap states where the lifetime is short. This results in faster recombination, hence R decreases. When P_{in} increases, D^* also decreases and I_{dark} remains unchanged. Figure 5(b) shows a monotonically increasing figure of merit with increasing forward bias potential of the device at a given incident power density (52.4 mW/cm^2).

The generation mechanism of photo-current can be understood in terms of (MóSóM) architecture as illustrated in figure S2(a). For electron transfer, charge carriers must overcome Schottky potential barriers created at semiconductor-metal interfaces. The choice of metal plays a significant role in the electrical contacts on the height of the Schottky barrier, here we have chosen the Aluminum metal for electrical contacts due to its work function ($\phi = 4.5 \text{ eV}$) nearly equal to the WS_2 work function ($\phi = 4.6 \text{ eV}$)⁴². Since the Schottky barrier acts as a current rectifier, the electron can move from semiconductor to metal and is controlled by two sides of the interface in equilibrium (contact barrier height) if there is no external effect on the system. Under dark conditions and without applying any bias voltage, the device exhibits a symmetric Schottky structure under the same vacuum level. Under illumination and without bias voltage, the barrier height depend on the generation and recombination of photo-generated charge carriers, when the photodetector devices absorb the light. The excitation of an electron or other charge carriers to a higher energy state produces an electrical potential separation in the metal-semiconductor junction and the photocurrent can take a direction. Application of positive bias voltage changes Schottky barrier height along with the direction and magnitude of the photocurrent schematically as shown in Figure S2(b). Under both bias voltage and illumination, the photo-generated charge carries start distribution at metal/ semiconductor interfaces. Depending on the charge accumulation process, the Schottky barrier height of the two interfaces tends to

vary further. Photo-excitation and application of biasing potential allows the magnitude of the electric field to increase further.

The switching response of the fabricated photodetector was measured at 2 Hz of excitation frequency with 405 nm illumination (power = 0.06 mW/cm²) as shown in Figure S3 (Supplementary information). We observed an on/off ratio of 10³ at biasing voltage of 5V upon 405 nm excitation. The observed switching time of T_{rise} = 0.20 sec and T_{fall} = 0.07 sec is faster than the previous report by J. D. Yao et al. in year, 2015 at biasing of 1V²⁵. For the PLD-grown WS₂, under vacuum conditions, they observed a switching time of T_{rise} = 9.9 sec and T_{fall} = 8.7 sec. The comparison of the key photodetector performance parameters reported by various researchers for WS₂ based PDs and Silicon PDs (for comparison purpose) has been enlisted in Table-I (Supplementary information). Typically the photoresponse time of Si based photodetectors ranges in the range 0.2-5.9 μs much faster than the observed photoresponse time of WS₂ based photodetectors (~few milli-seconds), While WS₂ based photodetectors, shows much higher responsivity 290-3106 AW⁻¹ (Our work and Yang, R. et al, *ACS applied materials & interfaces* **2017**) as compared to Si based photodetectors 0.14 AW⁻¹⁴³. The device exhibits internal gain because of the difference of the recombination lifetime and transit time⁴⁴. Since the electrons travel faster than holes and the recombination lifetime is very long, during transport in photodetectors electron completes its trips sooner than the hole.

In summary, monolayered continuous WS₂ was grown by atmospheric pressure CVD having crystallite size of ~80 μm using single zone furnace. Photodetector based on it showed responsivity of 290 AW⁻¹ at incident power density of 0.06 mW/cm² and excitation wavelength of 405 nm. For the first time such high responsivity has been observed in CVD grown monolayered WS₂ sample. We also observed faster switching time of about 10³-10⁴ μs for our

CVD grown samples as compared to previous reports. Defect concentration and grain boundaries impregnated during growth of WS₂ limits their switching time. Observed comparable switching time of $\sim 10^3 \mu\text{s}$ and high detectivity ($D = 52 \times 10^{14}$) indicates good quality of the samples and possibility of realizing efficient photodetectors based on monolayered WS₂ grown by atmospheric pressure CVD.

ACKNOWLEDGMENT

Dilip K. Singh thanks UGC-DAE CSR Indore (CRS/2021-22/01/358), NM-ICPS ISI Kolkata and DST, Government of India (CRG/2021/002179; CRG/2021/003705) for financial support. Prof. Dai-Sik Kim thanks National Research Foundation of Korea (NRF), Korea government (MIST) for the grant (NRF-2015R1A3A2031768 NRF-2022M3H4A1A04096465). We are also thankful to the CIF, BIT Mesra, INUP programme of IIT Guwahati and UNIST Central Research Facilities (UCRF) for the support of their facilities and equipment.

References

- (1) Fowler, B.; Liu, C.; Mims, S.; Balicki, J.; Li, W.; Do, H.; Appelbaum, J.; Vu, P. A 5.5 Mpixel 100 frames/sec wide dynamic range low noise CMOS image sensor for scientific applications. In *Sensors, Cameras, and Systems for Industrial/Scientific Applications XI*, 2010; SPIE: Vol. 7536, pp 58-69.
- (2) Kim, S.; Lim, Y. T.; Soltesz, E. G.; De Grand, A. M.; Lee, J.; Nakayama, A.; Parker, J. A.; Mihaljevic, T.; Laurence, R. G.; Dor, D. M. Near-infrared fluorescent type II quantum dots for sentinel lymph node mapping. *Nature biotechnology* **2004**, *22* (1), 93-97.
- (3) Formisano, V.; Atreya, S.; Encrenaz, T.; Ignatiev, N.; Giuranna, M. Detection of methane in the atmosphere of Mars. *science* **2004**, *306* (5702), 1758-1761.

- (4) Lussani, F. C.; Vescovi, R. F. d. C.; Souza, T. D. d.; Leite, C. A.; Giles, C. A versatile x-ray microtomography station for biomedical imaging and materials research. *Review of Scientific Instruments* **2015**, *86* (6), 063705.
- (5) Koppens, F.; Mueller, T.; Avouris, P.; Ferrari, A.; Vitiello, M.; Polini, M. Photodetectors based on graphene, other two-dimensional materials and hybrid systems. *Nature nanotechnology* **2014**, *9* (10), 780-793.
- (6) Wang, Q. H.; Kalantar-Zadeh, K.; Kis, A.; Coleman, J. N.; Strano, M. S. Electronics and optoelectronics of two-dimensional transition metal dichalcogenides. *Nature nanotechnology* **2012**, *7* (11), 699-712.
- (7) Luo, W.; Cao, Y.; Hu, P.; Cai, K.; Feng, Q.; Yan, F.; Yan, T.; Zhang, X.; Wang, K. Gate Tuning of High-Performance InSe-Based Photodetectors Using Graphene Electrodes. *Advanced Optical Materials* **2015**, *3* (10), 1418-1423.
- (8) Cao, Y.; Cai, K.; Hu, P.; Zhao, L.; Yan, T.; Luo, W.; Zhang, X.; Wu, X.; Wang, K.; Zheng, H. Strong enhancement of photoresponsivity with shrinking the electrodes spacing in few layer GaSe photodetectors. *Scientific reports* **2015**, *5* (1), 1-7.
- (9) Zhang, K.; Zhang, T.; Cheng, G.; Li, T.; Wang, S.; Wei, W.; Zhou, X.; Yu, W.; Sun, Y.; Wang, P. Interlayer transition and infrared photodetection in atomically thin type-II MoTe₂/MoS₂ van der Waals heterostructures. *ACS nano* **2016**, *10* (3), 3852-3858.
- (10) Wang, Y.; Zhou, W.-X.; Huang, L.; Xia, C.; Tang, L.-M.; Deng, H.-X.; Li, Y.; Chen, K.-Q.; Li, J.; Wei, Z. Light induced double spin state anti-ambipolar behavior and self-driven photoswitching in p-WSe₂/n-SnS₂ heterostructures. *2D Materials* **2017**, *4* (2), 025097.
- (11) Xia, F.; Wang, H.; Xiao, D.; Dubey, M.; Ramasubramanian, A. Two-dimensional material nanophotonics. *Nature Photonics* **2014**, *8* (12), 899-907.
- (12) Splendiani, A.; Sun, L.; Zhang, Y.; Li, T.; Kim, J.; Chim, C.-Y.; Galli, G.; Wang, F. Emerging photoluminescence in monolayer MoS₂. *Nano letters* **2010**, *10* (4), 1271-1275.
- (13) Mak, K. F.; Lee, C.; Hone, J.; Shan, J.; Heinz, T. F. Atomically thin MoS₂: a new direct-gap semiconductor. *Physical review letters* **2010**, *105* (13), 136805.
- (14) Amani, M.; Lien, D.-H.; Kiriya, D.; Xiao, J.; Azcatl, A.; Noh, J.; Madhvapathy, S. R.; Addou, R.; Kc, S.; Dubey, M. Near-unity photoluminescence quantum yield in MoS₂. *Science* **2015**, *350* (6264), 1065-1068.
- (15) Zhang, Z.; Chen, P.; Duan, X.; Zang, K.; Luo, J.; Duan, X. Robust epitaxial growth of two-dimensional heterostructures, multiheterostructures, and superlattices. *Science* **2017**, *357* (6353), 788-792.

- (16) Joensen, P.; Frindt, R.; Morrison, S. R. Single-layer mos2. *Materials research bulletin* **1986**, *21* (4), 457-461.
- (17) Novoselov, K. S.; Jiang, D.; Schedin, F.; Booth, T.; Khotkevich, V.; Morozov, S.; Geim, A. K. Two-dimensional atomic crystals. *Proceedings of the National Academy of Sciences* **2005**, *102* (30), 10451-10453.
- (18) Frindt, R.; Yoffe, A. Physical properties of layer structures: optical properties and photoconductivity of thin crystals of molybdenum disulphide. *Proceedings of the Royal Society of London. Series A. Mathematical and Physical Sciences* **1963**, *273* (1352), 69-83.
- (19) Mak, K. F.; Shan, J. Photonics and optoelectronics of 2D semiconductor transition metal dichalcogenides. *Nature Photonics* **2016**, *10* (4), 216-226.
- (20) Yin, Z.; Li, H.; Li, H.; Jiang, L.; Shi, Y.; Sun, Y.; Lu, G.; Zhang, Q.; Chen, X.; Zhang, H. Single-layer MoS₂ phototransistors. *ACS nano* **2012**, *6* (1), 74-80.
- (21) Liu, L.; Kumar, S. B.; Ouyang, Y.; Guo, J. Performance limits of monolayer transition metal dichalcogenide transistors. *IEEE Transactions on Electron Devices* **2011**, *58* (9), 3042-3047.
- (22) Bernardi, M.; Palummo, M.; Grossman, J. C. Extraordinary sunlight absorption and one nanometer thick photovoltaics using two-dimensional monolayer materials. *Nano letters* **2013**, *13* (8), 3664-3670.
- (23) Zhu, B.; Chen, X.; Cui, X. Exciton binding energy of monolayer WS₂. *Scientific reports* **2015**, *5* (1), 1-5.
- (24) Peimyoo, N.; Shang, J.; Cong, C.; Shen, X.; Wu, X.; Yeow, E. K.; Yu, T. Nonblinking, intense two-dimensional light emitter: monolayer WS₂ triangles. *ACS nano* **2013**, *7* (12), 10985-10994.
- (25) Yao, J.-D.; Zheng, Z.-Q.; Shao, J.; Yang, G. Stable, highly-responsive and broadband photodetection based on large-area multilayered WS₂ films grown by pulsed-laser deposition. *Nanoscale* **2015**, *7* (36), 14974-14981.
- (26) Hwan Lee, S.; Lee, D.; Sik Hwang, W.; Hwang, E.; Jena, D.; Jong Yoo, W. High-performance photocurrent generation from two-dimensional WS₂ field-effect transistors. *Applied Physics Letters* **2014**, *104* (19), 193113.
- (27) Huo, N.; Kang, J.; Wei, Z.; Li, S. S.; Li, J.; Wei, S. H. Novel and enhanced optoelectronic performances of multilayer MoS₂/WS₂ heterostructure transistors. *Advanced Functional Materials* **2014**, *24* (44), 7025-7031.
- (28) Gutiérrez, H. R.; Perea-López, N.; Elías, A. L.; Berkdemir, A.; Wang, B.; Lv, R.; López-Urías, F.; Crespi, V. H.; Terrones, H.; Terrones, M. Extraordinary room-temperature photoluminescence in triangular WS₂ monolayers. *Nano letters* **2013**, *13* (8), 3447-3454.

- (29) McCreary, K. M.; Hanbicki, A. T.; Jernigan, G. G.; Culbertson, J. C.; Jonker, B. T. Synthesis of large-area WS₂ monolayers with exceptional photoluminescence. *Scientific reports* **2016**, *6* (1), 1-7.
- (30) Kang, K.; Xie, S.; Huang, L.; Han, Y.; Huang, P. Y.; Mak, K. F.; Kim, C.-J.; Muller, D.; Park, J. High-mobility three-atom-thick semiconducting films with wafer-scale homogeneity. *Nature* **2015**, *520* (7549), 656-660.
- (31) Lan, C.; Li, C.; Yin, Y.; Liu, Y. Large-area synthesis of monolayer WS₂ and its ambient-sensitive photo-detecting performance. *Nanoscale* **2015**, *7* (14), 5974-5980.
- (32) Lan, C.; Zhou, Z.; Zhou, Z.; Li, C.; Shu, L.; Shen, L.; Li, D.; Dong, R.; Yip, S.; Ho, J. C. Wafer-scale synthesis of monolayer WS₂ for high-performance flexible photodetectors by enhanced chemical vapor deposition. *Nano Research* **2018**, *11* (6), 3371-3384.
- (33) Chen, Y. Growth of a large, single-crystalline WS₂ monolayer for high-performance photodetectors by chemical vapor deposition. *Micromachines* **2021**, *12* (2), 137.
- (34) Chen, Y.; Gan, L.; Li, H.; Ma, Y.; Zhai, T. Achieving uniform monolayer transition metal dichalcogenides film on silicon wafer via silanization treatment: a typical study on WS₂. *Advanced Materials* **2017**, *29* (7), 1603550.
- (35) Frey, G.; Tenne, R.; Matthews, M.; Dresselhaus, M.; Dresselhaus, G. Optical properties of MS₂ (M= Mo, W) inorganic fullerenelike and nanotube material optical absorption and resonance Raman measurements. *Journal of materials research* **1998**, *13* (9), 2412-2417.
- (36) Berkdemir, A.; Gutiérrez, H. R.; Botello-Méndez, A. R.; Perea-López, N.; Elías, A. L.; Chia, C.-I.; Wang, B.; Crespi, V. H.; López-Urías, F.; Charlier, J.-C. Identification of individual and few layers of WS₂ using Raman Spectroscopy. *Scientific reports* **2013**, *3* (1), 1-8.
- (37) Ballif, C.; Regula, M.; Schmid, P.; Rem-kar, M.; Sanjinés, R.; Lévy, F. Preparation and characterization of highly oriented, photoconducting WS₂ thin films. *Applied Physics A* **1996**, *62* (6), 543-546.
- (38) Hu, P.; Ye, J.; He, X.; Du, K.; Zhang, K. K.; Wang, X.; Xiong, Q.; Liu, Z.; Jiang, H.; Kloc, C. Control of radiative exciton recombination by charge transfer induced surface dipoles in MoS₂ and WS₂ monolayers. *Scientific reports* **2016**, *6* (1), 1-8.
- (39) Fang, Y.; Armin, A.; Meredith, P.; Huang, J. Accurate characterization of next-generation thin-film photodetectors. *Nature Photonics* **2019**, *13* (1), 1-4.
- (40) Sze, S. M.; Li, Y.; Ng, K. K. *Physics of semiconductor devices*; John Wiley & sons, 2021.

(41) Choi, W.; Cho, M. Y.; Konar, A.; Lee, J. H.; Cha, G. B.; Hong, S. C.; Kim, S.; Kim, J.; Jena, D.; Joo, J. High-detectivity multilayer MoS₂ phototransistors with spectral response from ultraviolet to infrared. *Advanced materials* **2012**, *24* (43), 5832-5836.

(42) Britnell, L.; Ribeiro, R. M.; Eckmann, A.; Jalil, R.; Belle, B. D.; Mishchenko, A.; Kim, Y.-J.; Gorbachev, R. V.; Georgiou, T.; Morozov, S. V. Strong light-matter interactions in heterostructures of atomically thin films. *Science* **2013**, *340* (6138), 1311-1314.

(43) Monroy, E.; Omnès, F.; Calle, F. Wide-bandgap semiconductor ultraviolet photodetectors. *Semiconductor science and technology* **2003**, *18* (4), R33.

(44) Dan, Y.; Zhao, X.; Chen, K.; Mesli, A. A photoconductor intrinsically has no gain. *Acs Photonics* **2018**, *5* (10), 4111-4116.

Figures:

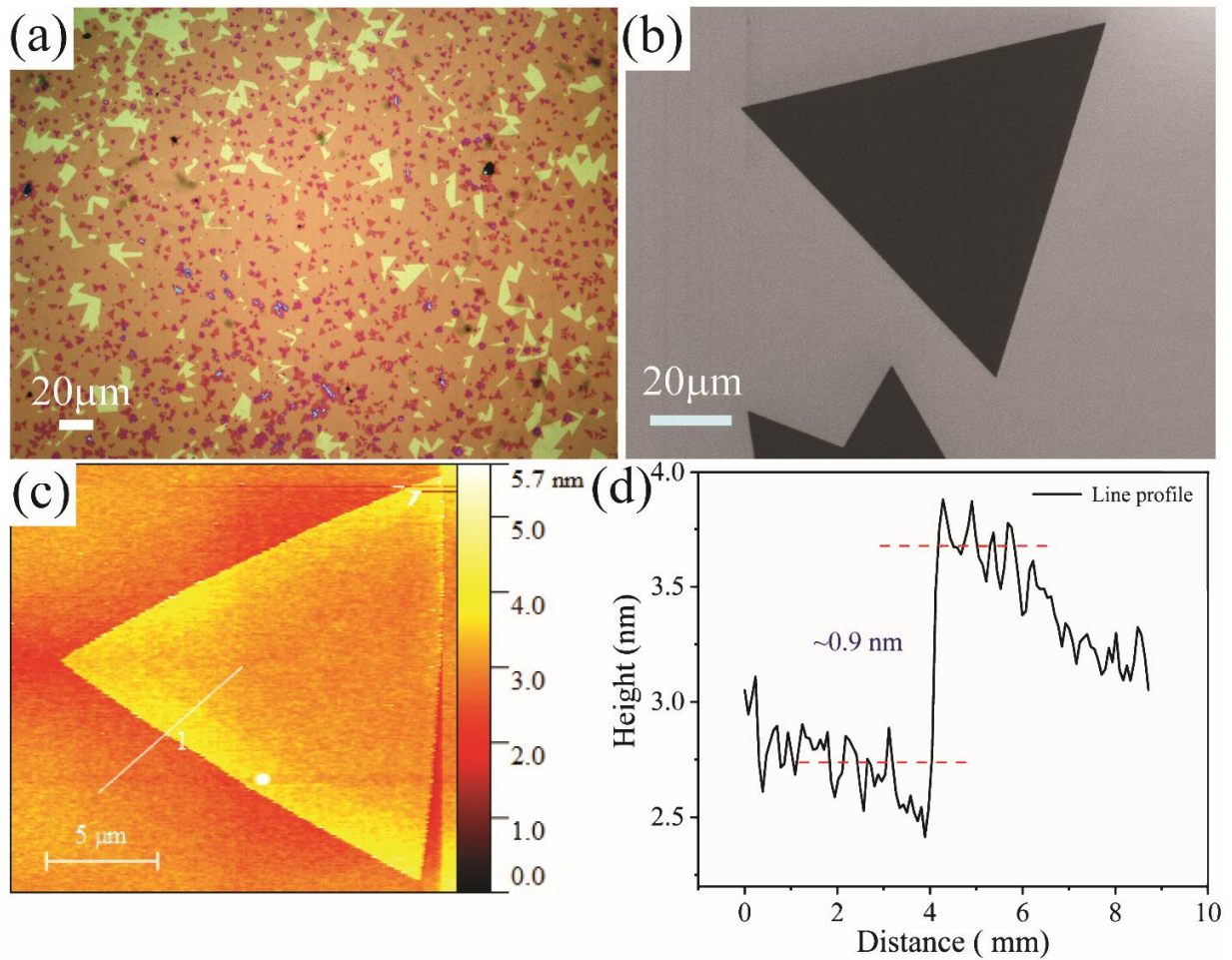


Figure.1 (a) Shows optical micrograph of a grown continuous layer of WS_2 and (b) FESEM image of one of the isolated crystals of WS_2 (c) Atomic Force Microscope (AFM) image of single layer of WS_2 (d) Thickness profile of WS_2 isolated crystal showing height = 0.9 nm indicating monolayer growth.

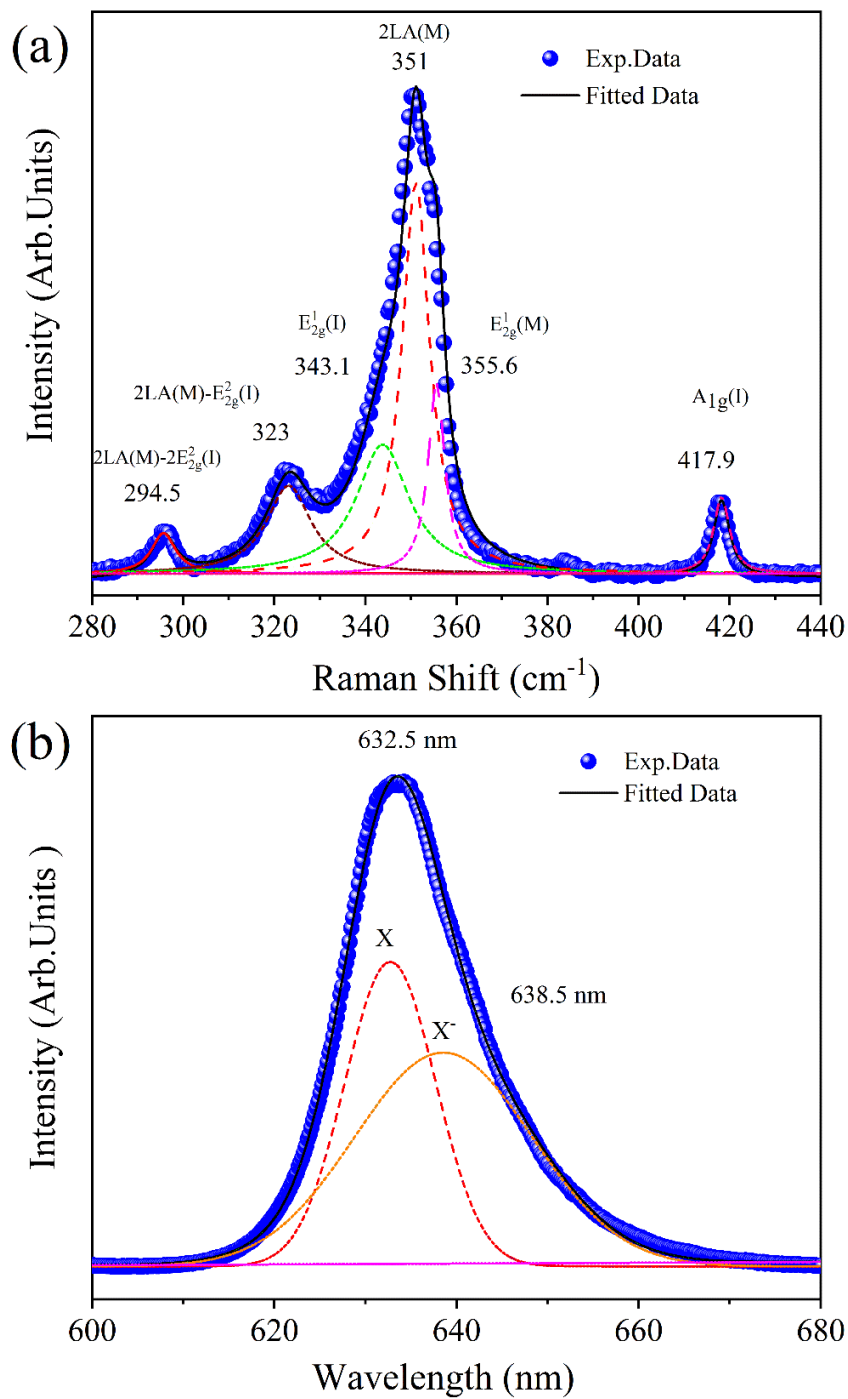


Figure.2 (a) shows the Raman Spectra and (b) Photoluminescence spectra of the monolayer WS₂ grown sample.

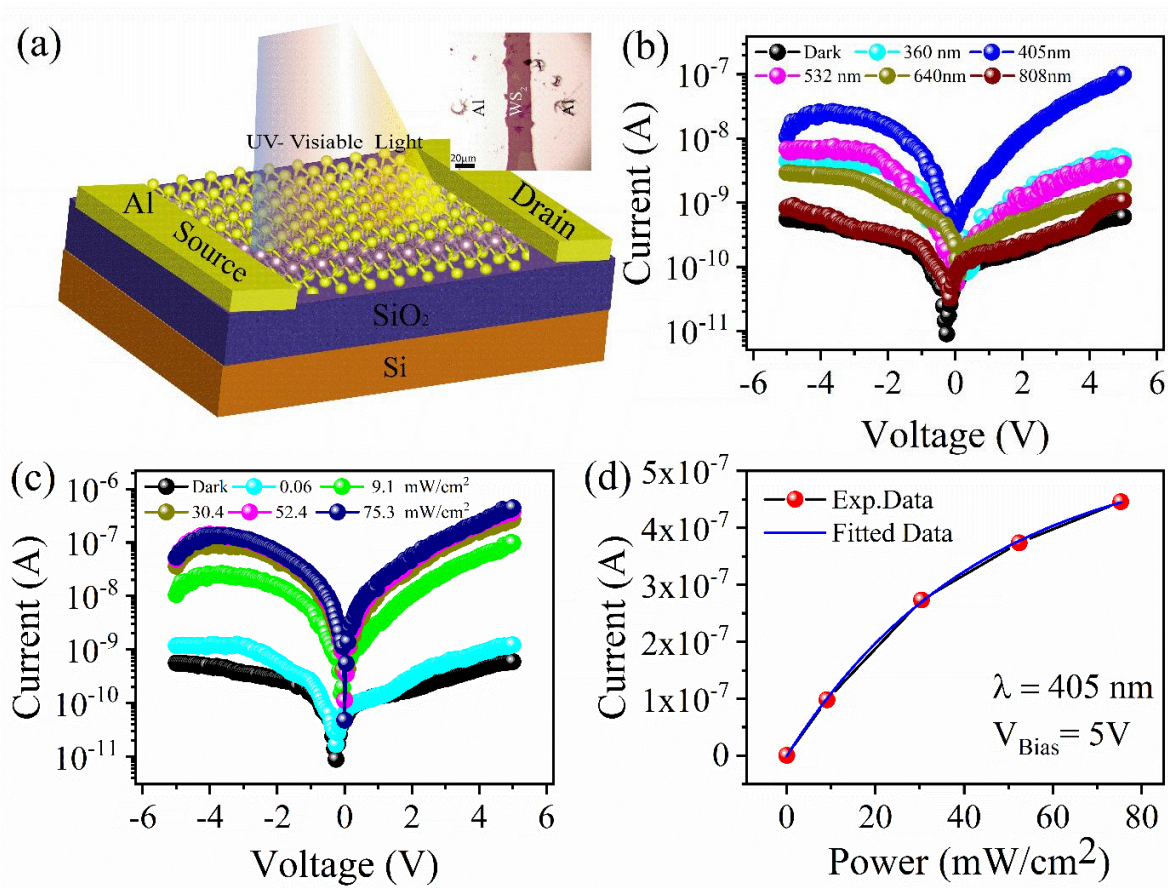


Figure.3(a) schematic diagram and optical Microscopy image of devices (b) I-V plot with different wavelength of laser source (c) I-V plot with varying incident intensity (under dark and upon 405 nm laser excitation) (d) logarithmic plot of the photo-current as a function of laser power intensity and fitted with power law for photodetector at a bias voltage of 5V.

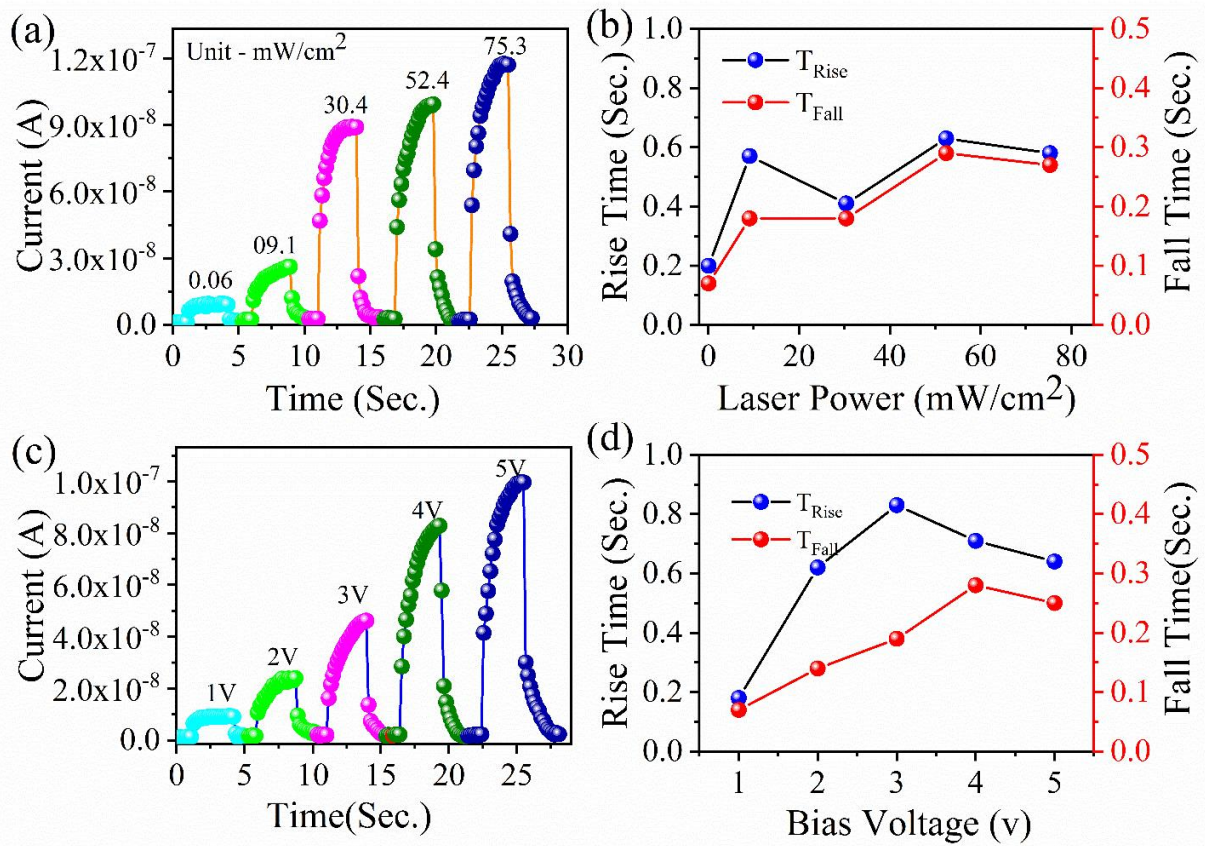


Figure.4 (a) Photocurrent response with different illumination varying laser power density with fixed bias voltage 5V. (b) Change in Rise and fall time of photo current response with respect to the variation of pulse laser power density. (c) Voltage-dependent photocurrent response under fixed laser excitation of a 405 nm laser. (d) Change in Rise and fall time of Photo current response with respect to the variation in bias potential with constant illuminated laser power.

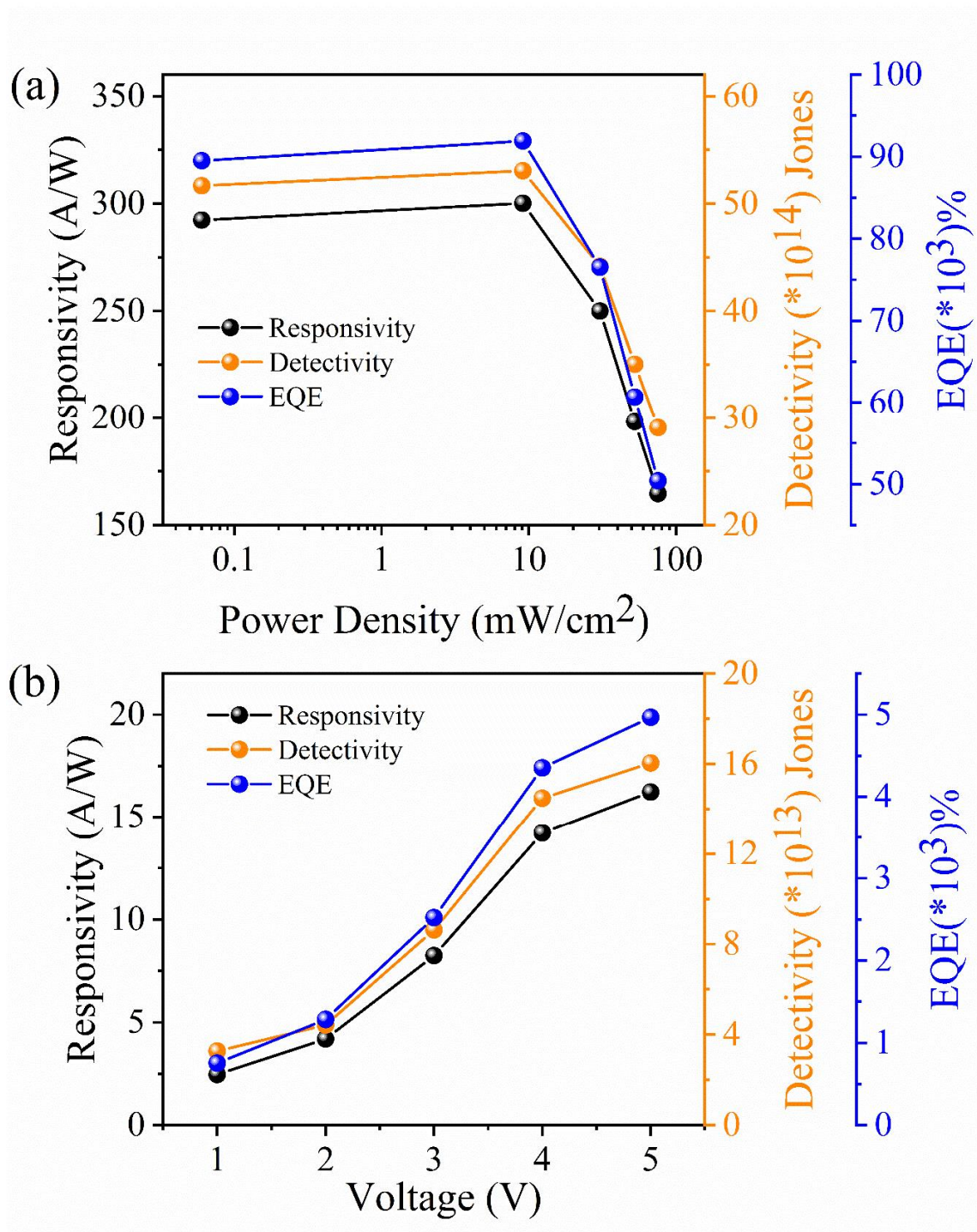


Figure.5 Responsivity, detectivity and EQE of the device as a function of (a) illumination intensity at wavelength 405 nm and (b) bias voltage.

Supplementary Information

High-Efficiency Photodetector Based On CVD-Grown WS₂ Monolayer

Rakesh K. Prasad¹, Koushik Ghosh², P. K. Giri², Dai-Sik Kim³, Dilip K. Singh^{1*}

¹Department of Physics, Birla Institute of Technology Mesra, Ranchi -835215, India

²Department of Physics, Indian Institute of Technology Guwahati, Assam-781039, India

³Department of Physics and Quantum Photonics Institute and Center for Atom Scale

Electromagnetism, Ulsan National Institute of Science and Technology (UNIST), Ulsan-44919,

Republic of Korea

*Email: dilipsinghnano1@gmail.com

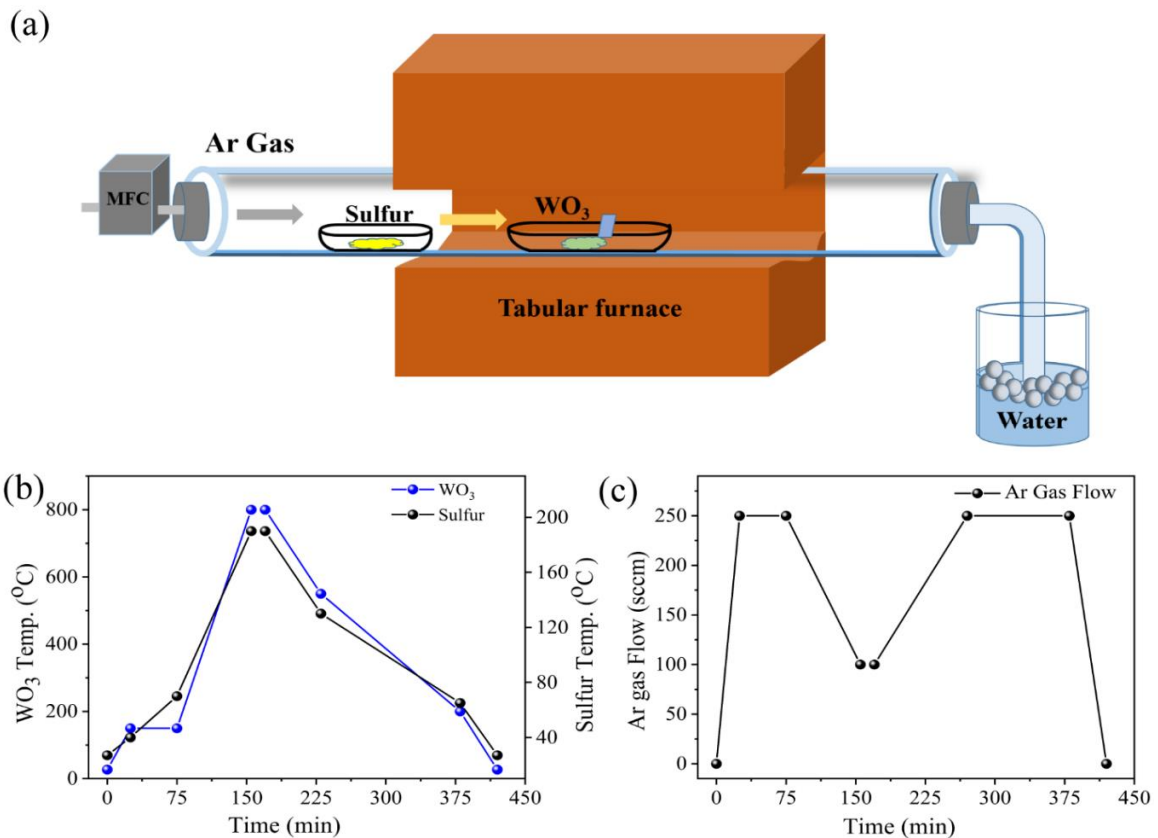


Figure S1 (a) Schematic diagram of Thermal CVD (b) Temperature and (c) Gas flow rate profile during the complete growth process.

Fig. S1 shows the schematic of the CVD setup used for growth. In CVD, the quartz tube of length 120 cm and diameter 4.5 cm was used. The temperature profile of both the precursors (WO_3 and S powder) during the complete cycle of growth has been shown in Fig. S1 (b) and the gas flow rate for the complete experimental duration. 285 nm SiO_2/Si wafer was used as a substrate for growth. The substrate was first cleaned sequentially using the isopropyl alcohol, water and ethanol through the sonication bath process for 15 min each. After sonication, the substrate was washed with deionized water and then dried using the argon gas and was placed inside the hot oven at 100 °C for 10 min. The polished surface of the substrate faces downward to the precursor above the WO_3 powder. Precursors and substrate were placed inside the CVD furnace as schematically shown in Fig. S1(a) separated at 19 cm. The outlet of the quartz tube was bubbled through a water bucket ensuring an equilibrium argon pressure inside the tube.

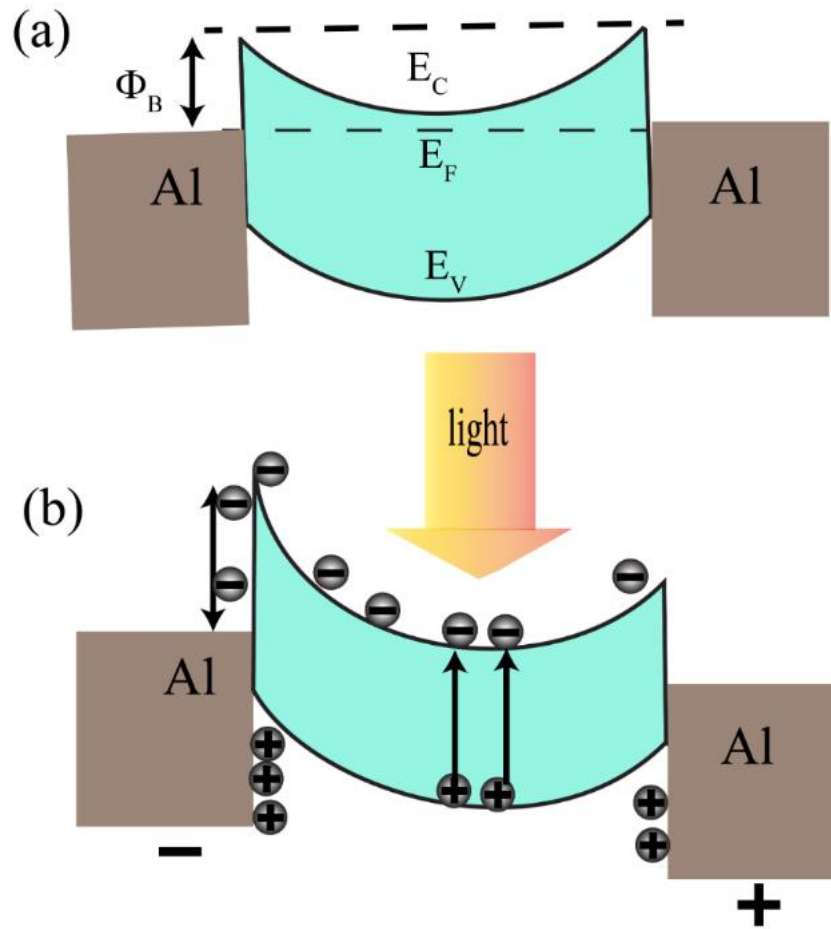


Fig. S2 Schematic diagram of mechanism of the photodetector (a) Without any bias and (b) with applied forward bias.

The band diagram for the metal-semiconductor-metal (M-S-M) contacts is schematically shown in Fig. S2

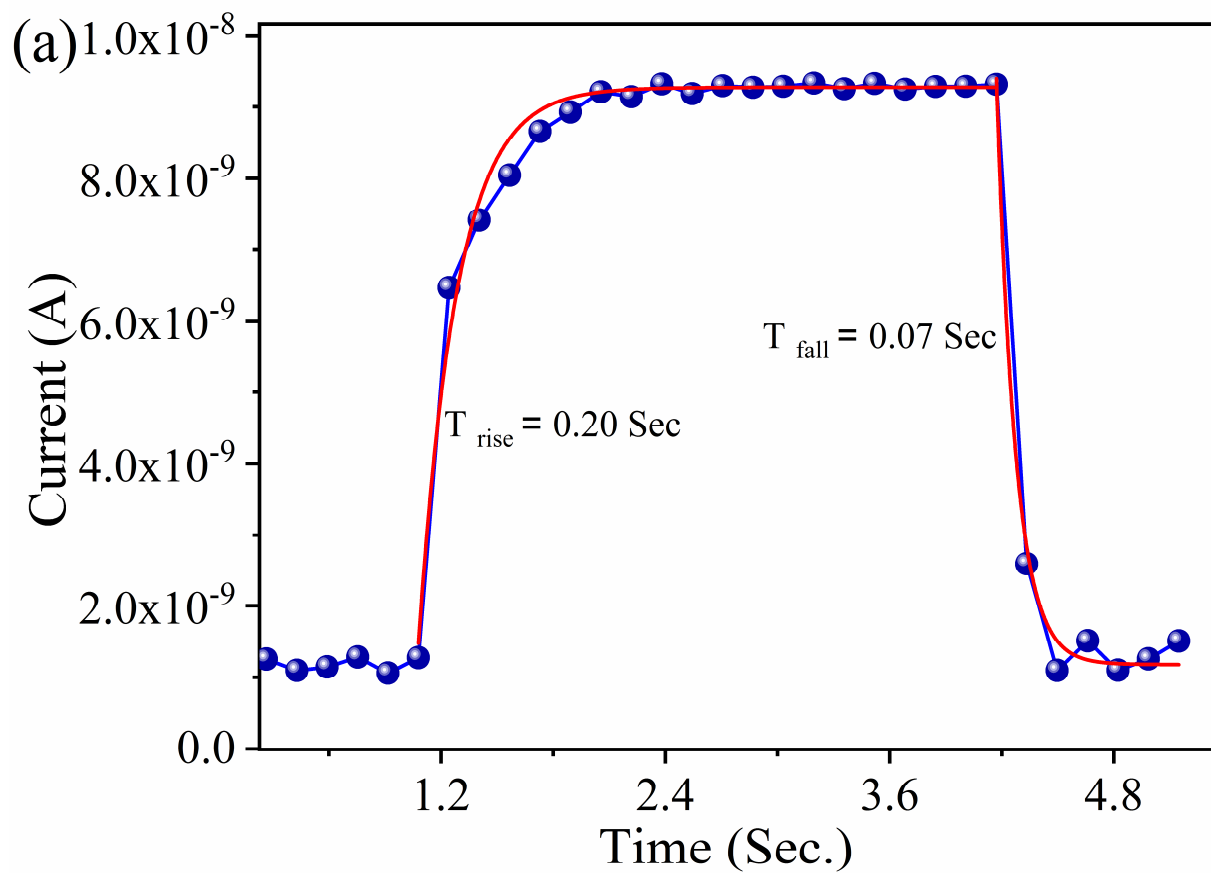


Figure S3: Rise Time (0.20 sec) and Fall Time (0.07 sec) of the device at 2Hz

Table-SI Comparison of the performance parameters of some common reference photodetectors based on Silicon, Ge and III-V nitrides and 2D-Semiconductors (MoS₂ and WS₂).

<i>No. of Layer</i>	<i>Measurement Condition</i>	<i>Responsivity (AW⁻¹)</i>	<i>Detectivity (D*)</i> <i>cm</i> <i>Hz^{1/2} W⁻¹</i>	<i>Response Time (μs)</i>	<i>Reference</i>
Si	= 254nm	0.14	N/A	0.2-5.9	¹
Si	= 850nm-900nm	N/A	~4×10 ¹³	N/A	²
Multilayer WS ₂	= 514nm	92 × 10 ⁻⁴	N/A	53 × 10 ²	³
Multilayer WS ₂ (PLD grown)	-	0.51 A W ⁻¹	2.7 × 10 ⁹	-	⁴
2L-WS ₂	V _{ds} = 1V V _g = 0V = 457nm P= 0.5 mWcm ⁻²	3106	5×10 ¹²	59(rise) 87(decay)	⁵
1l-WS ₂	V _{ds} = 10V V _g = 0V = 532nm P= 0.07 mWcm ⁻²	5.2×10 ⁻⁴	4.9×10 ⁹	< 560(rise) <560 (decay)	⁶
1L -WS ₂	V _{ds} = 20V V _g = 60V = 532nm P= 70 mW	0.019	N/A	6×10 ⁴ 1.9×10 ⁵	⁷
1L-WS ₂	= 500nm	3.07	N/A	37×10 ⁴	⁸
1L óWS ₂	= 405nm	290	52*10 ¹⁴	2.0 × 10 ⁴ 7.0 × 10 ³	Our work

References

- (1) Monroy, E.; Omnès, F.; Calle, F. Wide-bandgap semiconductor ultraviolet photodetectors. *Semiconductor science and technology* **2003**, *18* (4), R33.
- (2) Gong, X.; Tong, M.; Xia, Y.; Cai, W.; Moon, J. S.; Cao, Y.; Yu, G.; Shieh, C.-L.; Nilsson, B.; Heeger, A. J. High-detectivity polymer photodetectors with spectral response from 300 nm to 1450 nm. *Science* **2009**, *325* (5948), 1665-1667.
- (3) Elías, A.; Berkdemir, A.; Castro-Beltran, A.; Gutiérrez, H.; Feng, S.; Lv, R.; Hayashi, T.; López-Urías, F.; Ghosh, S.; Muchharla, B. Sensors: photosensor device based on few-layered WS₂ films. *Adv. Funct. Mater.* **2013**, *23* (44), 5511-5517.
- (4) Hwan Lee, S.; Lee, D.; Sik Hwang, W.; Hwang, E.; Jena, D.; Jong Yoo, W. High-performance photocurrent generation from two-dimensional WS₂ field-effect transistors. *Applied Physics Letters* **2014**, *104* (19), 193113.
- (5) Yang, R.; Feng, S.; Xiang, J.; Jia, Z.; Mu, C.; Wen, F.; Liu, Z. Ultrahigh-gain and fast photodetectors built on atomically thin bilayer tungsten disulfide grown by chemical vapor deposition. *ACS applied materials & interfaces* **2017**, *9* (48), 42001-42010.
- (6) Lan, C.; Zhou, Z.; Zhou, Z.; Li, C.; Shu, L.; Shen, L.; Li, D.; Dong, R.; Yip, S.; Ho, J. C. Wafer-scale synthesis of monolayer WS₂ for high-performance flexible photodetectors by enhanced chemical vapor deposition. *Nano Research* **2018**, *11* (6), 3371-3384.
- (7) Lan, C.; Li, C.; Yin, Y.; Liu, Y. Large-area synthesis of monolayer WS₂ and its ambient-sensitive photo-detecting performance. *Nanoscale* **2015**, *7* (14), 5974-5980.
- (8) Chen, Y.; Gan, L.; Li, H.; Ma, Y.; Zhai, T. Achieving uniform monolayer transition metal dichalcogenides film on silicon wafer via silanization treatment: a typical study on WS₂. *Advanced Materials* **2017**, *29* (7), 1603550